International Journal of Nanomedicine

Dovepress
Taylor & Francis Group

Open Access Full Text Article

ORIGINAL RESEARCH

Application of Cerium-Tannic Acid-Formaldehyde Coordination Polymer Colloidal Nanomaterials to Alleviate Lipopolysaccharide-Induced Acute Lung Injury

Xuanpeng Wu[1], Fei Xue[1], Dong Cheng[2–4], Leyu Hong[1], Chenxi Li[1], Ming Ni[1], Shuhao Liang[1], Tianhao Chen[1], Chao Luo[1], Jie Ren[5], Kunjin Wu[5], Tong Liu[6], Jingyao Zhang[6,7], Jing Wei[2–4], Chang Liu[5,7], Qifei Wu[1]

[1]Department of Thoracic Surgery, The First Affiliated Hospital of Xi'an Jiaotong University, Xi'an, 710061, People's Republic of China; [2]Institute of Analytical Chemistry and Instrument for Life Science, Xi'an Jiaotong University, Xi'an, 710049, People's Republic of China; [3]The Key Laboratory of Biomedical Information Engineering of Ministry of Education, Xi'an Jiaotong University, Xi'an, 710049, People's Republic of China; [4]School of Life Science and Technology, Xi'an Jiaotong University, Xi'an, 710049, People's Republic of China; [5]Department of Hepatobiliary Surgery and Liver Transplantation, The Second Affiliated Hospital of Xi'an Jiaotong University, Xi'an, 710004, People's Republic of China; [6]Department of Surgical Intensive Care Unit, The First Affiliated Hospital of Xi'an Jiaotong University, Xi'an, 710061, People's Republic of China; [7]The Key Laboratory of Surgical Critical Care and Life Support of Ministry of Education, Xi'an Jiaotong University, Xi'an, 710061, People's Republic of China

Correspondence: Chang Liu, Department of Hepatobiliary Surgery and Liver Transplantation, The Second Affiliated Hospital of Xi'an Jiaotong University, Xi'an, 710004, People's Republic of China, Email liuchangfh@xjtu.edu.cn; Qifei Wu, Department of Thoracic Surgery, The First Affiliated Hospital of Xi'an Jiaotong University, Xi'an, 710061, People's Republic of China, Email wuqifei-1@163.com

Background: Acute lung injury (ALI) is a severe respiratory disease worldwide and is characterized by a high mortality rate. Effective therapeutic interventions remain limited. Although metal-polyphenol coordination polymers (MPCPs) have shown considerable therapeutic potential across diverse pathological conditions, their application in ALI, along with the elucidation of the molecular mechanisms, remains insufficiently explored.

Methods: Based on the coordination interaction between cerium (Ce) and tannic acid (TA), a Ce-TA nanomaterial was synthesized through a facile and cost-effective method. The properties, stability, radical scavenging activity, and enzyme-like activity of Ce-TA were evaluated. Comprehensive assessments of its therapeutic effects and biosafety were performed using various cell models and a lipopolysaccharide (LPS)-induced ALI mouse model.

Results: Ce-TA exhibited ultrasmall size and high colloidal stability, efficiently scavenging multiple free radicals via its superoxide dismutase (SOD)-like and catalase (CAT)-like enzyme activities. Ce-TA inhibited H_2O_2-induced apoptosis and ROS production in BEAS-2B cells and human umbilical vein endothelial cells (HUVECs). Compared with the LPS group, Ce-TA effectively alleviated LPS-induced ALI by ameliorating lung histopathological injury, decreasing lung wet/dry weight (W/D) ratio, myeloperoxidase (MPO) and malondialdehyde (MDA) levels, and reducing inflammatory cytokine levels in vivo via activation of the PI3K/AKT/Nrf2 signaling pathway.

Conclusion: Ce-TA demonstrated significant anti-inflammatory and antioxidant effects both in vivo and in vitro, with confirmed safety for long-term application. It alleviated LPS-induced ALI by activating the PI3K/AKT/Nrf2 signaling pathway. The facile and economical synthesis of Ce-TA highlights its potential for clinical application, and these advantages make it a promising therapeutic agent for ALI.

Keywords: cerium-based nanomaterials, metal-polyphenol coordination polymers, acute lung injury, oxidative stress, ROS scavenging

Introduction

As a spectrum of severe respiratory diseases, acute lung injury (ALI) and acute respiratory distress syndrome (ARDS) represent a prevalent and critical clinical challenge worldwide. Characterized by acute pulmonary inflammation, the mortality rate of ALI is 30%-40% and the therapeutic strategies remain limited.[1] The primary therapeutic approach for

https://doi.org/10.2147/IJN.S604112
Received: 2 March 2026
Accepted: 1 June 2026
Published: 16 June 2026

ALI/ARDS is mainly symptomatic, involving mechanical ventilation and fluid management.[2] Drugs that alleviate inflammation, such as corticosteroids, have been regarded as potentially effective treatments for ARDS patients. However, the efficacy remains controversial, and there are currently no clear and standardized guidelines for their application.[3] The morbidity and mortality rates of ALI/ARDS are still high due to the current lack of effective clinical therapies. Therefore, treating ALI/ARDS presents a significant challenge that demands further investigation into effective therapeutic strategies and their underlying mechanisms.

Nano-coordinated polymers (NCPs) are generally defined as nanomaterials formed by coordination-driven self-assembly of metal ions or clusters with ligands. Characterized by customizable organic ligands and metal species, various morphologies and structures, and adjustable particle sizes, NCPs have been used as potential drug delivery platforms and therapeutic agents for multiple diseases.[4–6] Metal-polyphenol coordination polymers (MPCPs) represent a class of multifunctional organic materials formed by the coordination between metal ions and plant polyphenol ligands.[7,8] Plant polyphenols are one of the most abundant natural compounds with highly diverse chemical structures, which are widely present in various fruits, vegetables, and tea.[9,10] They are renowned for their broad pharmacological activities, including anti-inflammatory, antibacterial, antioxidant, anti-aging, and anti-cancer effects. Moreover, they have potent chelating abilities, enabling them to form stable MPCPs with a variety of metal ions, especially rare earth metal ions, via metal-catechol coordination bonds.[10–14] MPCPs can be engineered into multifunctional nanoplatforms, thereby enhancing therapeutic efficacy against various diseases.[15,16] They also exhibit excellent biocompatibility and negligible toxicity.[17,18] Our previous studies have shown that MPCPs exhibit great photothermal conversion performance, favorable dispersion and stability in aqueous solution, and other properties.[19,20] Based on these characteristics, MPCPs have attracted increasing attention in biomedical imaging, sensing, drug delivery and therapy.[21–24] Despite the application of MPCPs in various fields, research on MPCPs in the treatment of ALI remains limited.

Cerium nanoparticles exhibit unique chemical and physical properties. These particles can attenuate inflammatory and autoimmune responses, and possess antibacterial,[25] antiviral properties,[26] and additional advantages such as outstanding catalytic performance and optical properties, which have attracted extensive interest in various fields such as biomedicine. Cerium nanoparticles have been mainly used in ROS-related diseases, including heart disease, Alzheimer's disease (AD), and cancer, as potential therapeutic agents capable of providing sustained antioxidant effects.[27] Xu et al[28] engineered a brain-targeting cerium nanoparticle (T-CeNP), which demonstrated a capacity to scavenge excess reactive oxygen species (ROS) and suppress microglial activation, thereby delaying the progression of AD in a mouse model. Tannic acid (TA) is a natural polyphenolic compound with remarkable antioxidant and anti-inflammatory efficacy, which has attracted considerable interest for its application.[29] Leveraging these properties, Fu et al[30] developed a tannic acid-cerium nanozyme (TA-Ce) capable of protecting against acute kidney injury through multiple mechanisms, including ROS elimination, anti-inflammatory responses, and inhibition of apoptotic pathways. A self-assembled nanozyme inflammation-response platform (CeTA-K1tkP) developed by Peng et al[31] displayed a notable capacity to scavenge ROS and had a broad-spectrum effect on inflammatory diseases. It was expected to play a therapeutic role in a variety of diseases, including viral pneumonia such as COVID-19, sepsis, enteritis and arthritis. The combined findings from these studies strongly support the therapeutic potential of novel cerium- and tannic acid-based nanomaterials in ALI management.

Despite the well-established antioxidant and anti-inflammatory properties of cerium-based and tannic acid-based nanomaterials, the exploration of their application in ALI remains limited, and their effects and mechanisms need to be further elucidated. Recent advancements in nanozyme design demonstrate the potential to integrate multiple enzyme activities into a single nanoscale platform, thereby facilitating the regulation of disease microenvironments.[32–34] Furthermore, MPCPs have been successfully utilized for targeted delivery and acid-triggered release.[35] These strategies have inspired the development of novel nanomaterials in the treatment of ALI, emphasizing the significance of ROS scavenging. Therefore, this study aims to synthesize a stable and biocompatible cerium-tannic acid-formaldehyde coordination polymer colloidal nanomaterial (Ce-TA) via a facile method, evaluate its ROS-scavenging and anti-inflammatory effects both in vitro and in vivo, and elucidate the precise mechanism by which Ce-TA activates the PI3K/AKT/Nrf2 signaling pathway to suppress oxidative stress and inflammation in ALI (Scheme 1). This study not only confirms the therapeutic potential of Ce-TA but also provides a potential direction for the development of nanomaterials in the treatment of ALI/ARDS.

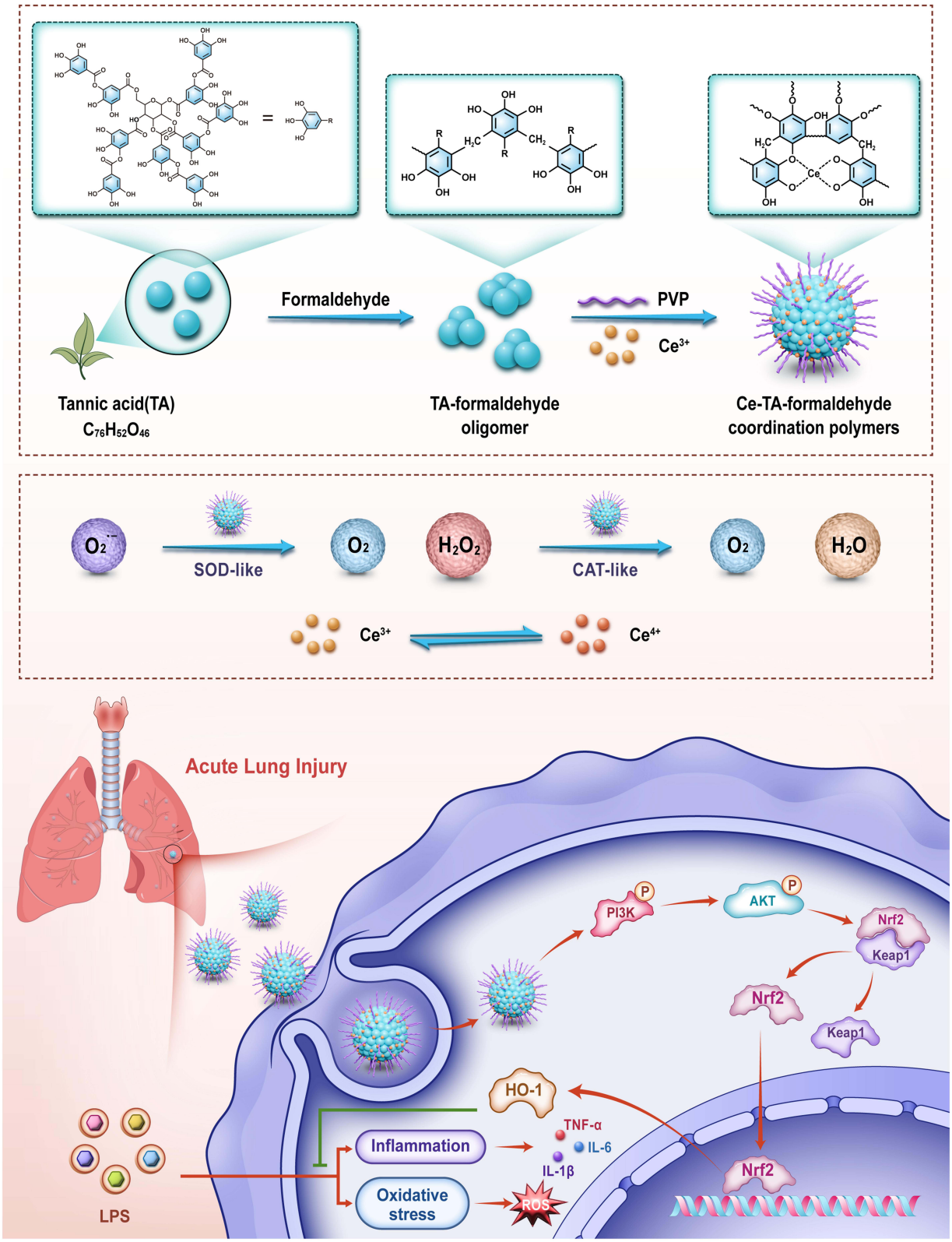

Scheme 1 Schematic illustration of the synthesis, dual enzyme-like activities, and therapeutic mechanism of Ce-TA nanoparticles.

https://doi.org/10.2147/IJN.S604112

Materials and Methods

Synthesis of Ce-TA

The cerium-tannic acid-formaldehyde coordination polymer colloidal nanoparticles were synthesized via a sol-gel process using TA as a ligand.[19,20] Typically, polyvinylpyrrolidone (PVP, 0.3 g) was dissolved in the mixture of water (37 mL), ethanol (8 mL, 99.5%) as well as ammonia (0.45 mL, 25 wt%). Subsequently, TA (0.2 g) was dissolved in the above solution followed by addition of formaldehyde solution (0.38 mL, 37 wt%). After 12 h, $Ce(NO_3)_3{\cdot}3H_2O$ aqueous solution (2 mL, 50 mg/mL) was added. After another 12 h, the solution was transferred to an autoclave for hydrothermal treatment at 100 °C for 12 h. The obtained products were dialyzed to remove the small molecules (eg., NH_4OH). The solid products were collected via a freeze-drying process. The obtained nanoparticles were named Ce-TA. TA (99%), PVP (Mw = 58 kg/mol, 99%), and $Ce(NO_3)_3{\cdot}3H_2O$ (99.99%) were purchased from Macklin Biochemical Co., Ltd. Ammonia solution, formaldehyde solution, and ethanol were purchased from Tianjin Zhiyuan Chemical Co., Ltd. All reagents were used without further purification.

Characterizations of Ce-TA

Dynamic light scattering (DLS) of Ce-TA was measured with Zetasizer Nano ZS (Malvern Instruments Ltd, UK). Transmission electron microscopy (TEM) images were taken by a JEM-F200 operated at an accelerating voltage of 200 kV. Atomic force microscope (AFM) images were collected using the ScanAsyst mode in air (Dimension Icon, Veeco Instruments/Bruker, Germany). Ultraviolet-visible-near infrared (UV-Vis-NIR) analysis was used to evaluate the optical characteristics of Ce-TA (Nanodrop 2000, Thermo Scientific, USA). The coordination between TA and metals was identified by Fourier transform infrared spectroscopy (FTIR, NicoletiS20, Thermo Scientific). The surface chemical composition and ionic valences were detected by X-ray photoelectron spectroscopy (XPS, K-Alpha, Thermo Scientific). The electron-spin-resonance (ESR) spectra were obtained using a Bruker EMXplus-6/1 spectrometer for the detection of hydroxyl radical and superoxide anion generation.

Radical Scavenging Ability, Superoxide Dismutase (SOD), and Catalase (CAT) Activities of Ce-TA

The ABTS radical (ml092656, mlbio, China), DPPH radical (BC4750, Solarbio, China), hydroxyl radical (·OH, ml076333, mlbio), and superoxide anion ($\cdot O_2^-$, ml0523652, mlbio) scavenging abilities, SOD (S0109, Beyotime, China) and CAT (BC0200, Solarbio) activities of Ce-TA were measured using different assay kits according to the manufacturer's instructions. Ce-TA at concentrations of 20-100 μg/mL was introduced into different assay kit working solutions. After sufficient reaction, the absorbance at different wavelengths was recorded using a microplate reader (1410101, Thermo Scientific), and subsequently converted to radical scavenging ability and enzyme activity.

Cell Culture and Treatment

BEAS-2B cells and human umbilical vein endothelial cells (HUVECs) were purchased from Hunan Fenghui Biotechnology Co., Ltd. (Hunan, China). BEAS-2B cells were cultured in Dulbecco's modified eagle medium (DMEM, Gibco, USA) containing 10% foetal bovine serum (FBS, Gibco, USA) and 1% penicillin/streptomycin under 5% CO_2 at 37 °C in an incubator. HUVECs were cultured in endothelial cell medium (ECM, ScienCell, USA) containing 5% FBS, 1% endothelial cell growth supplement (ECGS) and 1% penicillin/streptomycin under 5% CO_2 at 37 °C in an incubator.

Cell Counting Kit-8 (CCK-8) Assay

BEAS-2B cells and HUVECs were seeded in 96-well plates at a density of 1×10^4 cells per well. When the cells entered the logarithmic growth phase, the medium was discarded from the plate and culture media containing Ce-TA at different concentrations and 250 μM H_2O_2 were added to the wells. Cells treated with the same volume of normal medium were used as the control group. After incubation for 24 h at 37 °C and 5% CO_2, the medium was replaced with fresh medium containing 10% CCK-8 (C0039, Beyotime). The plates were protected from light and incubated at 37 °C for 4 h. Cell viability was determined using a microplate reader (1410101, Thermo Scientific) by measuring the absorbance at 450 nm.

Terminal Deoxynucleotidyl Transferase-Mediated dUTP Nick End Labeling (TUNEL) Staining

One step TUNEL apoptosis assay kit (C1090, Beyotime) was used to measure apoptosis. After treatment as described above, cells were washed with PBS and fixed with 4% paraformaldehyde (G1101, Servicebio, China) for 30 min, and then washed again with PBS. Next, cells were treated with PBS containing 0.3% Triton X-100 and incubated at room temperature for 5 min. The TUNEL detection solution was prepared according to the manufacturer's instruction. Cells were washed twice with PBS, then 50 μL of the TUNEL detection solution was added to each sample and incubated at 37 °C in the dark for 1 h. After incubation, cells were washed three times with PBS, treated with DAPI (1:4000, G1012, Servicebio) at room temperature for 8 min, blocked, and immediately observed under a fluorescence microscope (Axio Observer, ZEISS, Germany). For quantification, ImageJ software was used.

Detection of ROS Production in vitro

After the aforementioned treatment with H_2O_2 and different concentrations of Ce-TA for 24 h, the cells were rinsed three times with PBS to fully remove the treatment medium. A final concentration of 10 μM 2',7'-dichlorodihydrofluorescein diacetate (DCFH-DA, S0033S, Beyotime) in serum-free medium was added to the cells for ROS staining. The cells were incubated in the dark at 37 °C for 20 min. Then, the cells were washed with PBS three times to completely remove the free DCFH-DA dye. Afterward, the cells were imaged using a fluorescence microscope (Axio Observer, ZEISS). ImageJ software was used for quantification.

Flow Cytometry for Cell Apoptosis Detection

BEAS-2B cells were seeded in 6-well plates at a density of 1×10^5 cells per well and treated with H_2O_2 and Ce-TA as previously described. After incubation for 24 h, cells were washed three times with PBS and resuspended in 500 μL of binding buffer. Subsequently, 5 μL of Annexin V-FITC and 5 μL of PI (E-CK-A211, Elabscience, China) were added sequentially to the cell suspension, followed by incubation at room temperature in the dark for 15 min. Flow cytometric data were collected by a NovoCyte flow cytometer (Agilent, USA) and analyzed with FlowJo software.

Immunofluorescence Staining

BEAS-2B cells were treated with 10 μg/mL of lipopolysaccharide (LPS, L8880, Solarbio) for 24 h, followed by the addition of 100 μg/mL of Ce-TA for 24 h. Notably, LY294002 (30 μmol/mL, A133122, AmBeed, USA) was added 24 h before LPS treatment. The prepared cell slides were washed three times with PBS and fixed with 4% paraformaldehyde (G1101, Servicebio) at room temperature for 30 min, then incubated with 0.3% Triton X-100 for 3 min. After washing the slides with PBS three times, the cells were blocked with 10% BSA (A8010, Solarbio) for 30 min and incubated with primary antibodies (1:300, 80593-1-RR, Proteintech, China) at 4 °C overnight. The next day, the cells were incubated with fluorescent secondary antibodies (1:100, E-AB-1011, Elabscience) at room temperature for 60 min in the dark. Then DAPI (1:4000, G1012, Servicebio) staining was performed for 8 min. Finally, the cells were observed using a fluorescence microscope (Axio Observer, ZEISS). ImageJ software was used for quantification.

Animals

C57BL/6 mice (6–8 weeks, male, 20-25g) were purchased from GemPharmatech Co., Ltd. (Jiangsu, China), and were bred and raised in the animal room of Xi'an Jiaotong University Health Science Center. All animals underwent a one-week acclimatization period prior to the experiments.

LPS-Induced ALI Mice and Ce-TA Treatment Models

Mice were randomly divided into control and treatment groups, with each group having 5 animals. Mice were first anesthetized with 50 mg/kg of pentobarbital sodium (57-33-0, Merck, USA) by intraperitoneal injection (i.p.). Afterward, mice were intratracheally injected (i.t.) with 5 mg/kg LPS (L8880, Solarbio) to create ALI models. Mice were treated with Ce-TA or normal saline by intravenous injection (i.v.) or N-acetylcysteine (NAC, N800425, Macklin, China) by i.p.

at 6 h post-LPS injection. After intervention for 24 h, mice were euthanized by 150 mg/kg of pentobarbital sodium (i.v.), and bronchoalveolar lavage fluid (BALF) or lung tissues were collected subsequently.

Detection of ROS Production in vivo

Lung tissues were frozen and embedded in optimal cutting temperature (O.C.T.) specimen matrix for cryostat sectioning at -20 °C (Cryotome E, Thermo Scientific). Lung tissue sections were stained with 2 μg/mL of DAPI (G1012, Servicebio) and dihydroethidium (DHE, D7008, Servicebio) at 37 °C for 30 min. After three washes with PBS, sections were imaged using a fluorescence microscope (Axio Observer, ZEISS), and data were analyzed by ImageJ software.

BALF Cell Counting, Pro-Inflammatory Cytokines, Myeloperoxidase (MPO), and Protein Concentration Detection

White blood cells (WBCs) and neutrophil counts were obtained from the collected BALF using an automated hematology analyzer (pocH-100i, Sysmex, Japan) according to the manufacturer's protocols. Then, BALF was centrifuged at 3000 rpm for 10 min at 4 °C to obtain the supernatant. The levels of tumor necrosis factor alpha (TNF-α, ml002095, mlbio), interleukin 1β (IL-1β, ml301814, mlbio), interleukin 6 (IL-6, ml098430, mlbio), and MPO (ml002070, mlbio) in the BALF supernatant were measured using ELISA kits. The total protein concentration of the BALF supernatant was quantified using the bicinchoninic acid (BCA) protein assay kit (PQ003, Shaanxi ZHHC Biotechnology, China) according to the manufacturer's instructions.

Detection of SOD and Malondialdehyde (MDA) in Lung Tissues

Lung tissues were collected and homogenized using a tissue grinding instrument (KZ-II, Servicebio). The homogenates were then centrifuged at 4000 rpm for 15 min at 4 °C to obtain the supernatant. The activities of SOD and MDA were quantified using a SOD assay kit (S0101S, Beyotime) and an MDA assay kit (A003-1-2, Nanjing Jiancheng, China), respectively. The results were normalized to the total protein concentrations measured by the BCA protein assay.

Lung Wet/Dry Weight (W/D) Ratio

Lung tissues were collected and immediately weighed (wet weight) after residual blood on the surface was removed, and then dried in an oven at 60 °C for 72 h for dry weight measurement. Afterward, the W/D ratio was calculated to assess the severity of tissue edema.

Histopathological Evaluation

The organs were sampled, fixed with 4% paraformaldehyde (G1101, Servicebio) at room temperature for 24 h, and then dehydrated in an ethanol gradient. Then, organs were embedded in a wax block, and cut into 4 μm sections. Afterward, hematoxylin and eosin (H&E, G1005, Servicebio) staining was performed on the obtained sections, and pathological evaluation was done using a 3D slide microimaging system (DX12, 3DHistech, China). An independent investigator assessed the lung histopathology and was blinded to the group allocation. Lung injury was assessed based on four categories: interstitial inflammation, neutrophil infiltration, congestion and edema. A score of 0 to 4 was used to describe the severity of each category, with 0 representing minimal damage; 1 mild damage; 2 moderate damage; 3 severe damage; and 4 very severe damage. The lung injury score was determined by averaging the individual category scores, with each lung's result derived from the average of 10 high-power fields.

RNA Sequencing and Bioinformatics Analysis

Total RNA was extracted from lung tissues using an RNA-Quick Purification Kit (RN001, ES Science, China). RNA integrity was assessed on Bioanalyzer 2100 system (Agilent Technologies, CA, USA). Messenger RNA was purified from total RNA using poly-T oligo-attached magnetic beads. After fragmentation, the first strand cDNA was synthesized using random hexamer primers followed by the second strand cDNA synthesis. Sequencing libraries were prepared after end repair, A-tailing, adapter ligation, size selection, amplification, and purification. Libraries were checked with Qubit

and real-time PCR for quantification, and with a bioanalyzer for detecting the size distribution. After quality control, different libraries were pooled and subjected to Illumina sequencing (Illumina, San Diego, CA, USA). The sequencing was performed by Novogene (Beijing, China).

Differentially expressed genes were identified using DESeq2 R package (v1.20.0) with Benjamini-Hochberg-corrected p-value ≤ 0.05 and $|\log2(\text{fold change})| \geq 1$. Kyoto Encyclopedia of Genes and Genomes (KEGG) pathway enrichment analysis was performed using clusterProfiler R package (http://www.genome.jp/kegg/).

Quantitative Real-Time PCR (qPCR)

LY294002 (3 mg/mL, A133122, AmBeed, i.p.) was injected 2 h before LPS stimulation. LPS-induced ALI mice (5 mg/kg, i.t.) were treated with normal saline or Ce-TA (4 mg/kg, i.v.) at 6 h after LPS stimulation. After 24 h, mice were euthanized and lungs were collected. Total RNA from lung tissues was extracted using RNA-Quick Purification Kit (RN001, ES Science, China) according to the manufacturer's instructions. cDNA was synthesized using 1st Strand cDNA Synthesis SuperMix (11141ES60, Yeasen, China). The qPCR was performed using Fast SYBR qPCR Mix (A301-05, GenStar, China). The primer sequences were as follows: Nrf2: forward ATGATGGACTTGGAGTTGCC, reverse AAACTTGTACCGCCTCGTC; Keap1: forward CGGATGATCACACCGATGAATA, reverse CACACTGTTCAACTGGTCCT; HO-1: forward GACATGGCCT TCTGGTATGG, reverse CTCGTGGAGACGCTTTACATAG; and β-actin: forward CATCCGTAAAGACCTCTA TGCCAAC, reverse ATGGAGCCACCGATCCACA.

Western Blotting

For SDS-PAGE, a 10% separating gel, a 5% concentrated gel, an electrophoresis buffer, and a membrane transfer solution (precooled at 4 °C) were prepared and reserved until use. For SDS-PAGE electrophoresis, the samples were loaded according to the experimental requirements, the electrophoresis tank was filled with an electrophoresis buffer, and the voltage was adjusted to 90 V and increased to 130 V after 30 min. PVDF membranes (Merck Millipore, USA) were activated by immersion in methanol at a constant flow of 250 mA, and membrane transfer was carried out for 90 min. Then the membranes were blocked with 5% powdered skim milk at room temperature for 2 h and incubated with primary antibodies at 4 °C overnight, followed by incubation with HRP-conjugated goat anti-mouse (1:10000) or goat anti-rabbit IgG secondary antibodies (1:10000; both Servicebio). Membranes were incubated with enhanced chemiluminescence (ECL, 4AW011-200, 4A Biotech, China) solution. Finally, the membranes were visualized using the Tanon imaging system, and the blots were analyzed by ImageJ software. The following primary antibodies were used in this study: PI3K (1:5000, 60225-1-Ig, Proteintech), p-PI3K (1:1000, AF3242, Affinity, USA), AKT (1:5000, 60203-2-Ig, Proteintech), p-AKT (1:2000, 66444-1-Ig, Proteintech), Nrf2 (1:1000, 80593-1-RR, Proteintech), Keap1 (1:1000, R26935, Zen-Bio, China), HO-1 (1:1000, R380753, Zen-Bio), and β-actin (1:5000, YM8343, Immunoway, USA).

Immunohistochemical Staining

Mice were treated with LPS, Ce-TA, or LY294002 as previously mentioned After the lung tissues were collected, sections of paraffin blocks containing lung tissues were prepared The sections were dewaxed and treated with 3% H_2O_2 to inactivate the endogenous peroxidase, then blocked with 3% BSA (A8010, Solarbio). The sections were then incubated with anti-Nrf2 antibody (1:800, 80,593-1-RR, Proteintech) overnight at 4 °C. Finally, the slides were washed and incubated with HRP-conjugated secondary antibodies (1:500, GB23303, Servicebio). The sections were photographed under a 3D slide micro-imaging system (DX12, 3DHistech), and the positive areas were analyzed by ImageJ software.

Biocompatibility Evaluation of Ce-TA in Mice

Major organs (liver, kidney, spleen, heart, and lung) and blood samples of the control group and the 4 mg/kg Ce-TA (i.v.) group were harvested. The weights of mice from 0 to 28 d were recorded to draw the weight change curve.

Whole blood of mice was obtained by venous blood collection and stored in an anticoagulant tube containing EDTA, and then centrifuged at 3000 rpm for 15 min to separate red blood cells (RBCs). Afterward, 1mL Ce-TA at different concentrations, 1mL ultra-pure water (ddH_2O) and 1mL PBS solution were mixed with 20 μL blood cells respectively. Then, samples were incubated at 37 °C for 4 h and centrifuged at 3000 rpm for 15 min. The supernatant of the samples was transferred into the

96-well plate and the absorbance at 450 nm was detected. The hemolysis rate of Ce-TA was calculated using the following equation: Hemolysis (%) = [OD (Samples) – OD (PBS)] / [OD (ddH_2O) – OD (PBS)] × 100%.

Complete Blood Panel Analysis and Serum Biochemistry Test

Blood samples were collected and measured using an automatic hematology analyzer (BC-2800vet, Mindray, China). The remaining blood samples were then centrifuged at 3000 rpm for 15 min at 4 °C to isolate the serum. The serum was analyzed for critical biomarkers of hepatic and kidney functions, including alanine transaminase (ALT), aspartate transaminase (AST), creatinine (CREA), and blood urea nitrogen (BUN), using an automatic biochemical analyzer (7180, Hitachi, Japan).

Statistical Analysis

Comparisons among groups were analyzed using one-way ANOVA with Tukey's multiple comparisons test. Student's t-tests were performed to compare the differences between two groups. Statistical significance was set at $p<0.05$. Results are presented as mean ± standard deviation (SD). OriginPro (OriginPro v.2024, OriginLab Corporation, Northampton, MA, USA) and GraphPad Prism 9.5 software (GraphPad, San Diego, CA, USA) were used for statistical analysis and graphical generation.

Results

Synthesis and Characterization of Ce-TA

To develop Ce-TA nanomaterial for ALI therapy, we used a sol-gel method, which involved two main steps (Scheme 1). Firstly, TA reacted with formaldehyde under alkaline conditions to form TA-formaldehyde oligomer.[36] Cross-linking with formaldehyde makes the oligomer more stable Secondly, Ce^{3+} ions were added to trigger the metal-ligand coordination assembly. Polyvinylpyrrolidone (PVP) molecules were used in this process to prevent the aggregation of MPCP nanoparticles. As a result, Ce-TA nanoparticles with small diameter and high colloidal stability were successfully synthesized. Next, a comprehensive characterization of Ce-TA was performed. Transmission electron microscopy (TEM) images showed Ce-TA nanoparticles with an average size of around 22 nm (Figure 1A). Ce-TA nanoparticles were further characterized by atomic force microscope (AFM) (Figure 1B). The diameters of Ce-TA nanoparticles labeled in the AFM image were both 49 nm by calculation of the height of nanoparticles (Figure 1C). The hydrodynamic diameter of Ce-TA was measured by dynamic light scattering (DLS) (Figure 1D). Ce-TA exhibited a mean hydrodynamic diameter of 29 nm, which remained nearly constant (27 nm) after 30 d of storage. The photograph of Ce-TA in water (1 mg/mL) showed a clear solution, suggesting good dispersibility. After standing for 30 d, no precipitate was observed, indicating the high colloidal stability of Ce-TA in water (Figure 1E).

Ultraviolet-visible-near infrared (UV-Vis-NIR) absorption spectroscopy showed characteristic absorptions of TA at around 213 nm and 275 nm, while the peak shifted to 205 nm in Ce-TA due to the coordination of Ce^{3+} with the phenolic hydroxyl group of TA (Figure 2A). Fourier transform infrared spectroscopy (FTIR) revealed the characteristic absorption peaks corresponding to -OH at approximately 3450 cm^{-1} for both TA and Ce-TA.[37] TA exhibited absorption peaks at 1202 cm^{-1} and 1030 cm^{-1}, whereas Ce-TA displayed a peak at 1287 cm^{-1}, both related to stretching vibrations of C-O. Notably, the characteristic C=O absorption peak at 1649 cm^{-1} in Ce-TA may be associated with the presence of formaldehyde in the reaction system (Figure 2B). Furthermore, X-ray photoelectron spectroscopy (XPS) was performed to examine the elemental composition of Ce-TA and the valence state of the Ce ions.[31,38] The XPS spectrum of Ce-TA confirmed the coexistence of C, N, O, and Ce in the sample (Figure 2C). C 1s spectra showed two peaks centered at 284.8 eV (representing the C-C bond) and 287.73 eV (representing the C-O bond), respectively (Figure 2D). The presence of nitrogen atoms indicated the existence of PVP on the surface of Ce-TA. O 1s spectra showed two peaks centered at 529.66 eV (representing the C-O bond) and 531.36 eV (representing the C=O bond), respectively (Figure 2E). Moreover, Ce 3d spectra revealed characteristic peaks at 901, 898, 885, and 880 eV attributed to Ce 3d 3/2 and Ce 3d 5/2 of Ce (IV), whereas the peaks at 904 and 883 eV were

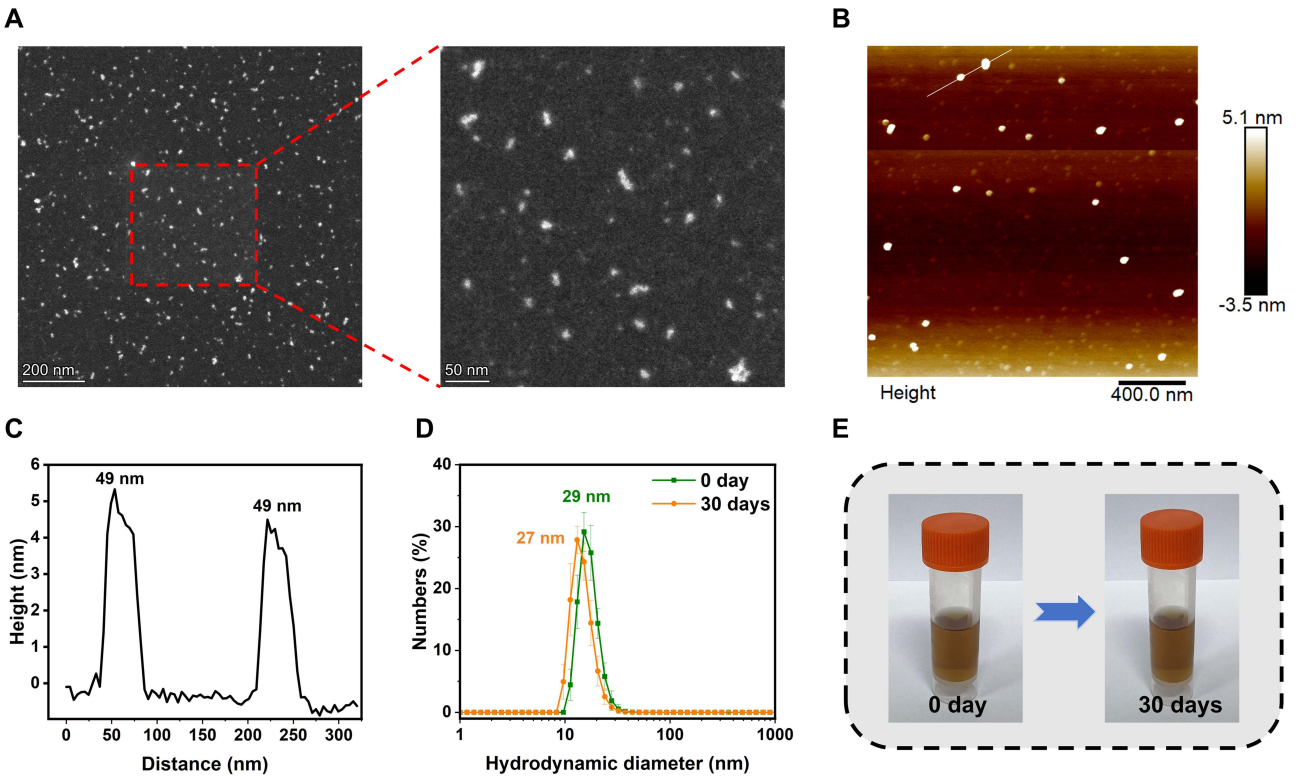

Figure 1 Characterization of Ce-TA. (**A**) TEM and (**B**) AFM images for Ce-TA. (**C**) The height profile along the line marked in the AFM image. (**D**) The hydrodynamic diameter distributions of Ce-TA solution on 0 and 30 d measured by DLS. (**E**) Photographs of Ce-TA solution on 0 and 30 d.

attributed to Ce 3d 3/2 and Ce 3d 5/2 of Ce (III); the estimated Ce (III) to Ce (IV) ratio was 1:2 (Figure 2F), suggesting the presence of predominantly the oxidation-resistant Ce^{4+} ions.[31,38]

Hydroxyl radical (·OH) and superoxide anion ($\cdot O_2^-$) are the two main types of ROS in cellular environments. We further investigated the scavenging ability of Ce-TA on ·OH and $\cdot O_2^-$ free radicals by electron-spin-resonance (ESR). According to the results, the addition of Ce-TA significantly reduced the spectral signals of ·OH and $\cdot O_2^-$ free radicals, confirming the excellent radical scavenging activities of Ce-TA (Figure 2G and H). In addition, we also used several reagent kits to detect the radical scavenging abilities of Ce-TA. The results showed that Ce-TA at concentrations of 20-100 μg/mL exhibited potent ABTS, DPPH, ·OH, and $\cdot O_2^-$ free radical scavenging abilities, as well as superoxide dismutase (SOD)-like and catalase (CAT)-like activities, and exhibited concentration-dependent activity (Figure 2I-L and Figure S1).

Biocompatibility and ROS Scavenging Ability of Ce-TA in vitro

Before evaluating the therapeutic effects, we first assessed the biocompatibility of Ce-TA in vitro using BEAS-2B cells and human umbilical vein endothelial cells (HUVECs). After incubation with various concentrations of Ce-TA for 24 h, cell viability was evaluated by cell counting kit-8 (CCK-8) assay. The results showed that Ce-TA exhibited no toxicity to BEAS-2B cells at concentrations up to 100 μg/mL, and HUVECs maintained high viability even at 200 μg/mL, demonstrating its favorable biocompatibility (Figure S2A and B). To assess the cytoprotective effect of Ce-TA against ROS, terminal deoxynucleotidyl transferase dUTP nick end labeling (TUNEL) staining results revealed that Ce-TA significantly reduced H_2O_2-induced apoptosis in both cell types (Figure 3A), with quantitative analysis confirming these results (Figure 3E and F). 2',7'-dichlorodihydrofluorescein diacetate (DCFH-DA) staining showed significantly lower ROS levels in cells treated with both H_2O_2 and Ce-TA compared to H_2O_2 alone (Figure 3C), and quantitative data confirmed the outstanding ROS-scavenging ability of Ce-TA (Figure 3G and H). Furthermore, CCK-8 assays and apoptosis flow cytometry analysis showed that Ce-TA significantly improved cell viabilities following H_2O_2 exposure (Figure 3B, D, and I). Together, these findings suggest that Ce-TA alleviates oxidative stress and protects BEAS-2B cells and HUVECs from ROS damage.

https://doi.org/10.2147/IJN.S604112

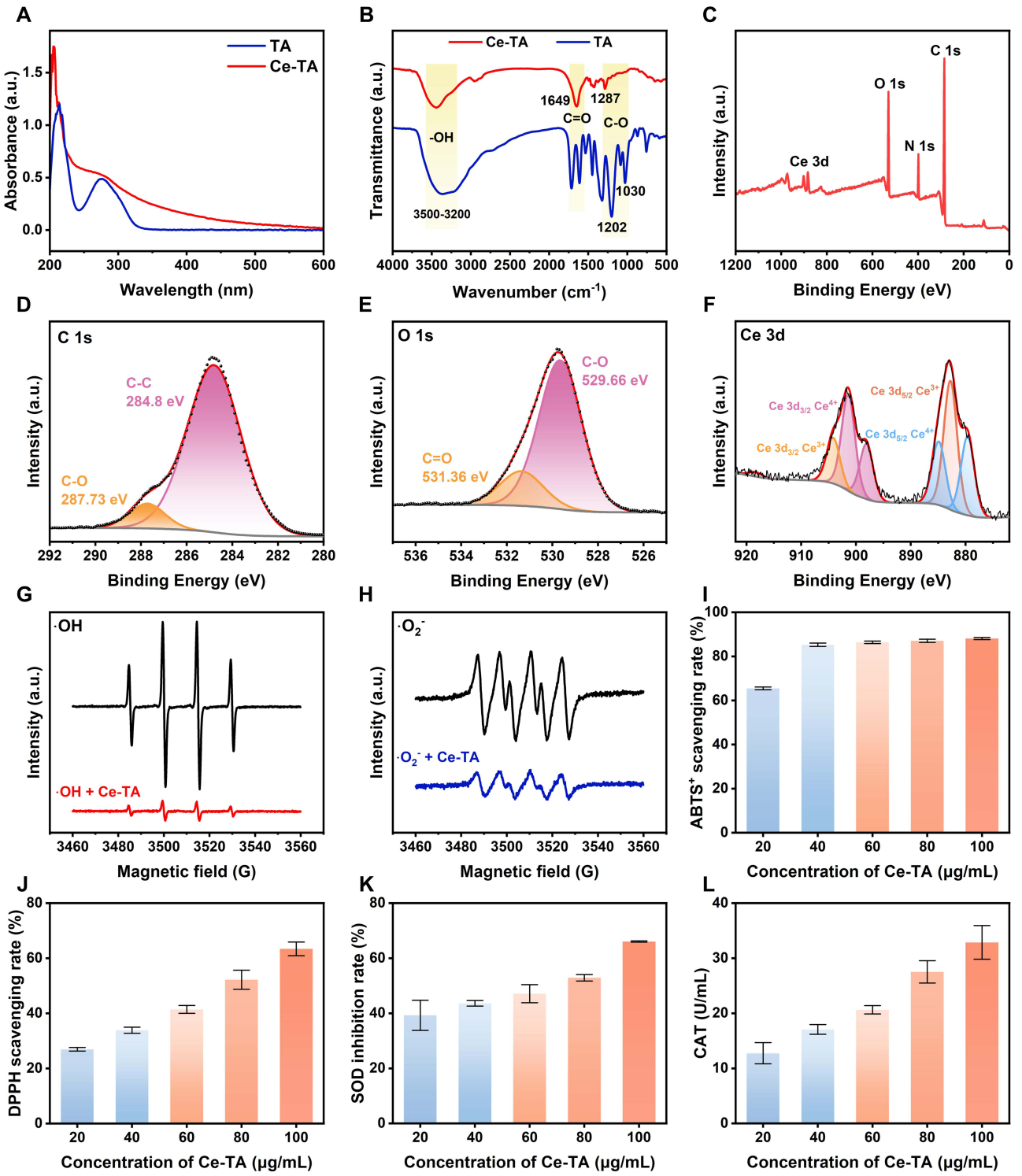

Figure 2 Characterization of Ce-TA. (**A**) UV-Vis-NIR absorbance of TA and Ce-TA. (**B**) FTIR spectra of TA and Ce-TA. (**C**) XPS analysis of Ce-TA. (**D**) C 1s, (**E**) O 1s, and (**F**) Ce 3d XPS spectra of Ce-TA. ESR spectra of Ce-TA reacted with (**G**) ·OH and (**H**) $\cdot O_2^-$ free radicals. (**I**) $ABTS^+$ and (**J**) DPPH scavenging abilities of Ce-TA at different concentrations. (**K**) SOD and (**L**) CAT activities of Ce-TA at different concentrations. Data are presented as means ± SD.

Ce-TA Reduced Oxidative Stress in Lipopolysaccharide (LPS)-Induced ALI Mice

After confirming the ROS scavenging ability of Ce-TA in vitro, we further evaluated its antioxidant efficacy in an LPS-induced ALI mouse model to determine whether Ce-TA could reduce oxidative stress in vivo. C57BL/6 mice were intratracheally injected (i.t.) with LPS (5 mg/kg) to induce ALI, and then intravenously injected (i.v.) with normal saline,

https://doi.org/10.2147/IJN.S604112

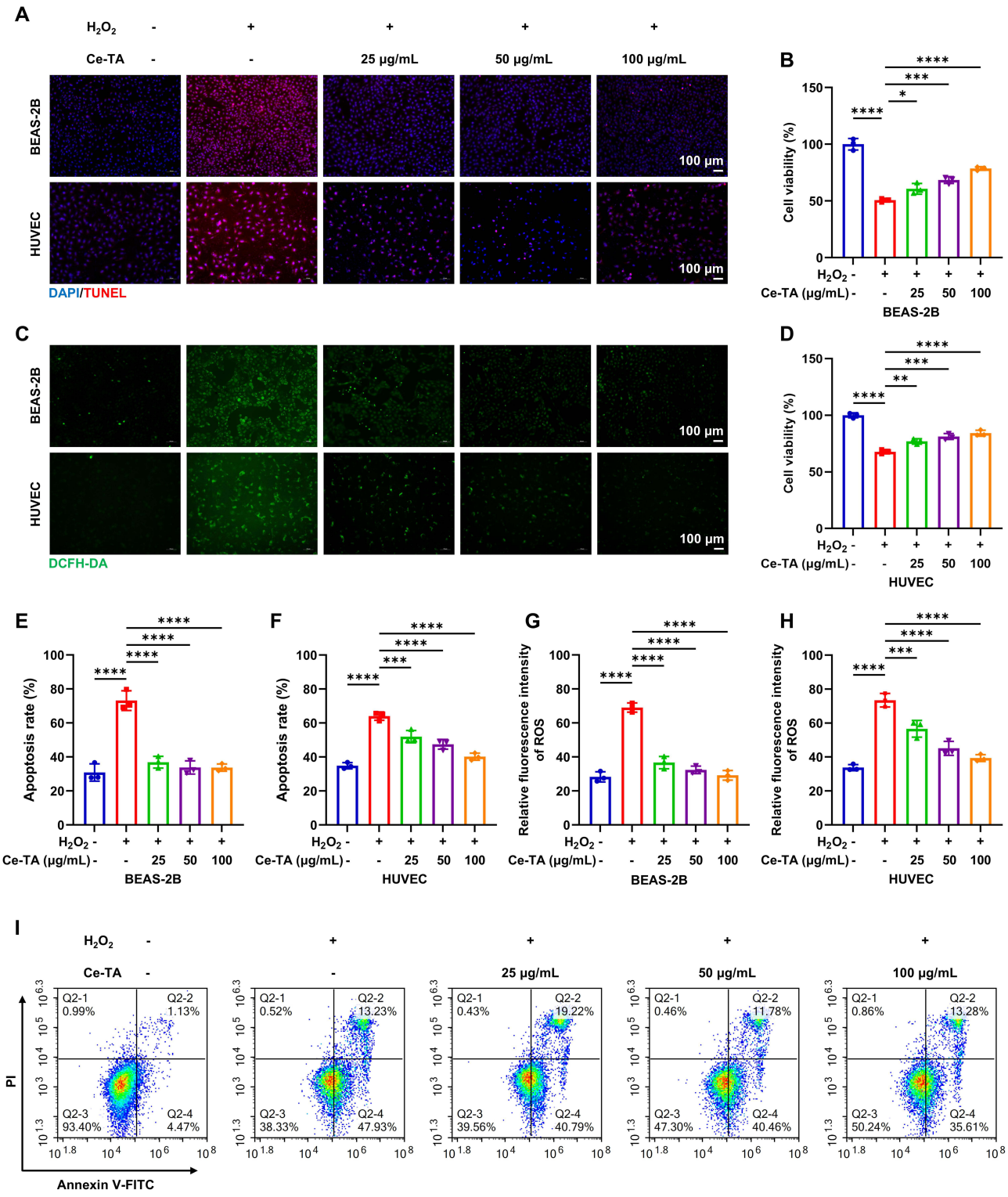

Figure 3 ROS scavenging and anti-apoptosis abilities of Ce-TA in vitro on BEAS-2B cells and HUVECs. (**A**) Representative TUNEL fluorescence images of BEAS-2B cells and HUVECs. (**B**) Cell viability of BEAS-2B cells under different treatment conditions. (**C**) Representative DCFH-DA fluorescence images of BEAS-2B cells and HUVECs. (**D**) Cell viability of HUVECs under different treatment conditions. Quantitative analysis of the proportion of TUNEL-positive cells in (**E**) BEAS-2B cells and (**F**) HUVECs under different treatment conditions. Quantitative analysis of the relative fluorescence intensity of the ROS level in (**G**) BEAS-2B cells and (**H**) HUVECs under different treatment conditions. (**I**) Cell apoptosis of BEAS-2B cells detected by flow cytometry under different treatment conditions. Data are presented as means ± SD (n = 3 per group). *$p < 0.05$, **$p < 0.01$, ***$p < 0.001$, ****$p < 0.0001$.

https://doi.org/10.2147/IJN.S604112

low dose (1 mg/kg), or high dose (4 mg/kg) of Ce-TA at 6 h after LPS stimulation. The conventional antioxidant drug (NAC, 1 g/kg) was intraperitoneally injected (i.p.) to serve as the positive control.[39] Bronchoalveolar lavage fluid (BALF) or lung tissues were collected at 24 h post-treatments (Figure 4A). Dihydroethidium (DHE) staining and quantitative analysis revealed that ROS generation in lung tissues was significantly inhibited in Ce-TA-treated groups compared with normal saline group, demonstrating the potent in vivo antioxidant activity of Ce-TA (Figure 4B and C).

Myeloperoxidase (MPO), superoxide dismutase (SOD), and malondialdehyde (MDA) are important markers to evaluate the level of oxidative stress. As shown in Figure 4D, the concentration of MPO in BALF was evidently reduced after the mice were treated with Ce-TA and NAC. Similarly, SOD activities in the lung tissues of the Ce-TA-treated groups were significantly higher than those of the normal saline-treated group (Figure 4E). MDA activities were significantly decreased after Ce-TA treatment (Figure 4F). Consequently, these results substantiate that Ce-TA attenuates oxidative stress by scavenging ROS, implicating its therapeutic potential in ALI.

Ce-TA Attenuated Inflammatory Response and Alleviated LPS-Induced Injury in ALI Mice

Given that excessive ROS could trigger endothelial and epithelial barrier dysfunction, and contribute to the development of ALI, we investigated whether Ce-TA could attenuate pulmonary inflammation and pathological damage. As shown in Figure 5A and B, LPS treatment significantly increased white blood cell (WBC) and neutrophil counts in BALF compared to the control group. After treated with Ce-TA or NAC, the WBCs and neutrophils in BALF were significantly reduced compared to the normal saline-treated group. These findings were consistent with the results obtained previously (Figure 4D), given that MPO is mainly expressed in neutrophils.[40] In addition, ELISA assays revealed that Ce-TA treatment substantially suppressed the LPS-induced elevation of key pro-inflammatory cytokines in BALF, including TNF-α, IL-1β, and IL-6 (Figure 5C-E). These results confirmed the ability of Ce-TA in alleviating pulmonary inflammation in ALI.

Next, we measured the protein concentration in BALF to evaluate the therapeutic effect of Ce-TA on alveolar-capillary barrier dysfunction. As shown in Figure 5F, Ce-TA significantly reduced the protein level in BALF compared to the normal saline-treated group. Lung wet/dry (W/D) ratio demonstrated that Ce-TA treatment significantly ameliorated pulmonary edema (Figure 5G). Further hematoxylin and eosin (H&E) staining showed obvious infiltration of inflammatory cells, alveolar edema and collapse, and disappearance of the alveolar cavity in normal saline-treated ALI mice. However, these alterations were significantly reversed by Ce-TA and NAC, as the lung tissue structure was nearly normal (Figure 5I and J). Lung injury score also confirmed the above results (Figure 5H). Consequently, these results provided direct evidence that Ce-TA may have a therapeutic effect on lung tissue damage in LPS-induced ALI.

Elucidating the Therapeutic Mechanism of Ce-TA

To explore the therapeutic mechanisms of Ce-TA, we performed RNA sequencing in an LPS-induced ALI mouse model. The Venn diagram revealed 5231 differentially expressed genes between the control group and LPS group, and 495 between the Ce-TA-treated group and LPS group, with 520 shared between the two comparisons (Figure 6A). Volcano plots showed 642 upregulated and 373 downregulated genes in Ce-TA-treated group compared with the LPS + Ce-TA group (Figure 6B). Kyoto Encyclopedia of Genes and Genomes (KEGG) pathway enrichment analysis indicated that the PI3K/AKT, JAK-STAT, and chemokine signaling pathways were associated with the therapeutic mechanisms of Ce-TA (Figure 6C). This finding was consistent with our previous results that Ce-TA could attenuate lung inflammation.

Transcriptomic results highlighted the PI3K/AKT signaling pathway as central to the therapeutic mechanism of Ce-TA. As a major regulator of cellular homeostasis, Nrf2 coordinates multiple protective processes including redox balance, metabolic stability, proteostasis and intracellular iron dynamics.[41] A previous study demonstrated that activation of the PI3K/AKT/Nrf2 pathway inhibited inflammation and apoptosis, thereby attenuating LPS-induced acute kidney injury.[42] Zhou et al[43] reported that coptisine (COP) mitigated ALI by alleviating ferroptosis through the PI3K/AKT/Nrf2 pathway. Based on these and our previous findings, we speculated that Ce-TA may exert anti-inflammatory and antioxidant effects through PI3K/AKT/Nrf2 and its downstream signaling pathways.

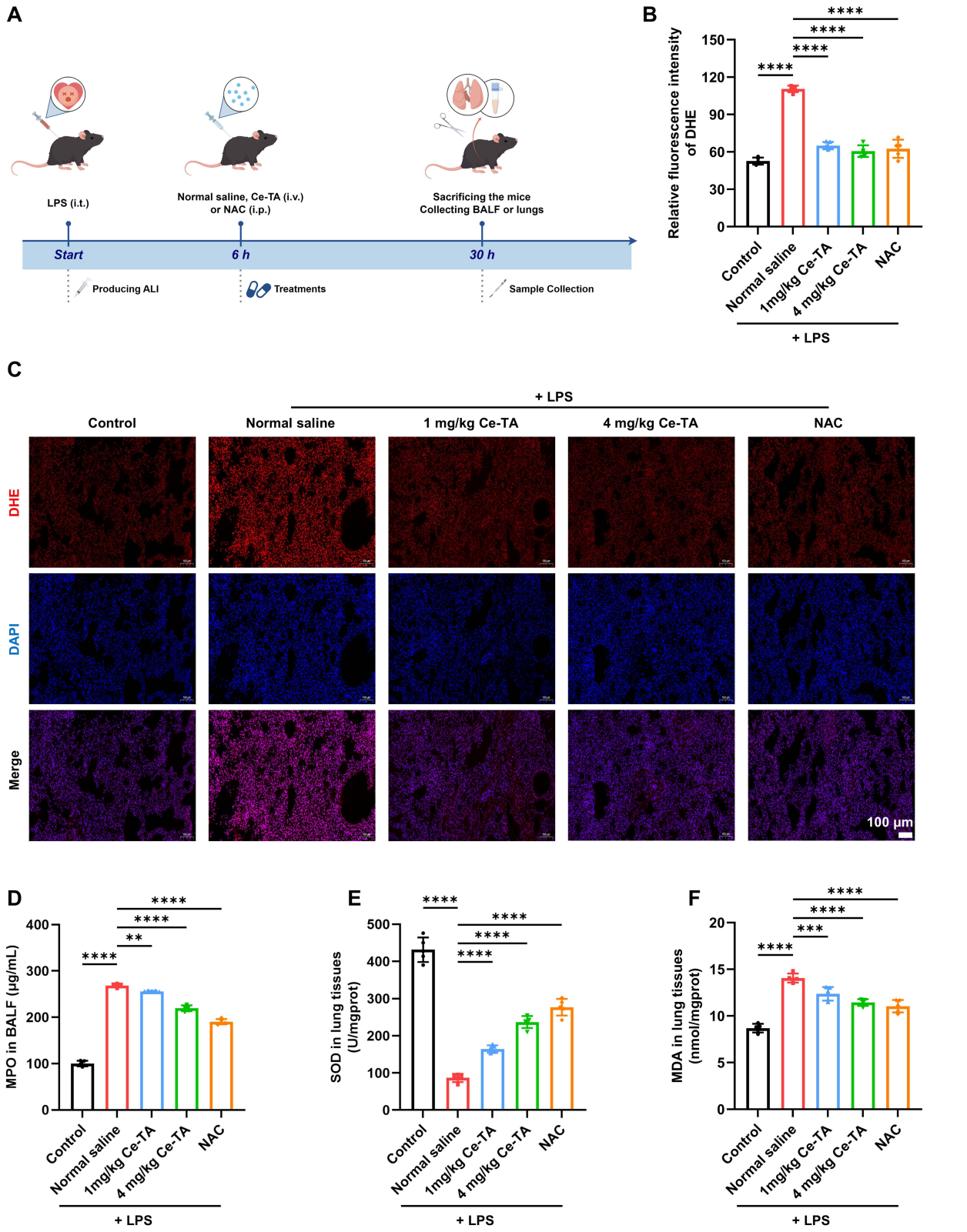

Figure 4 Antioxidant effect of Ce-TA on LPS-induced ALI mice. (**A**) Schematic illustration of the establishment and treatment schedule of LPS-induced ALI mice. (**B**) Quantitative analysis of the relative fluorescence intensity of DHE in lung tissues of mice in different groups. (**C**) Representative DHE fluorescence images of lung tissues of mice in different groups. (**D**) Concentration of MPO in BALF of mice in different groups. Concentrations of (**E**) SOD and (**F**) MDA in lung homogenates of mice in different groups. Data are presented as means ± SD (n = 5 per group). $^{**}p < 0.01$, $^{***}p < 0.001$, $^{****}p < 0.0001$.

https://doi.org/10.2147/IJN.S604112

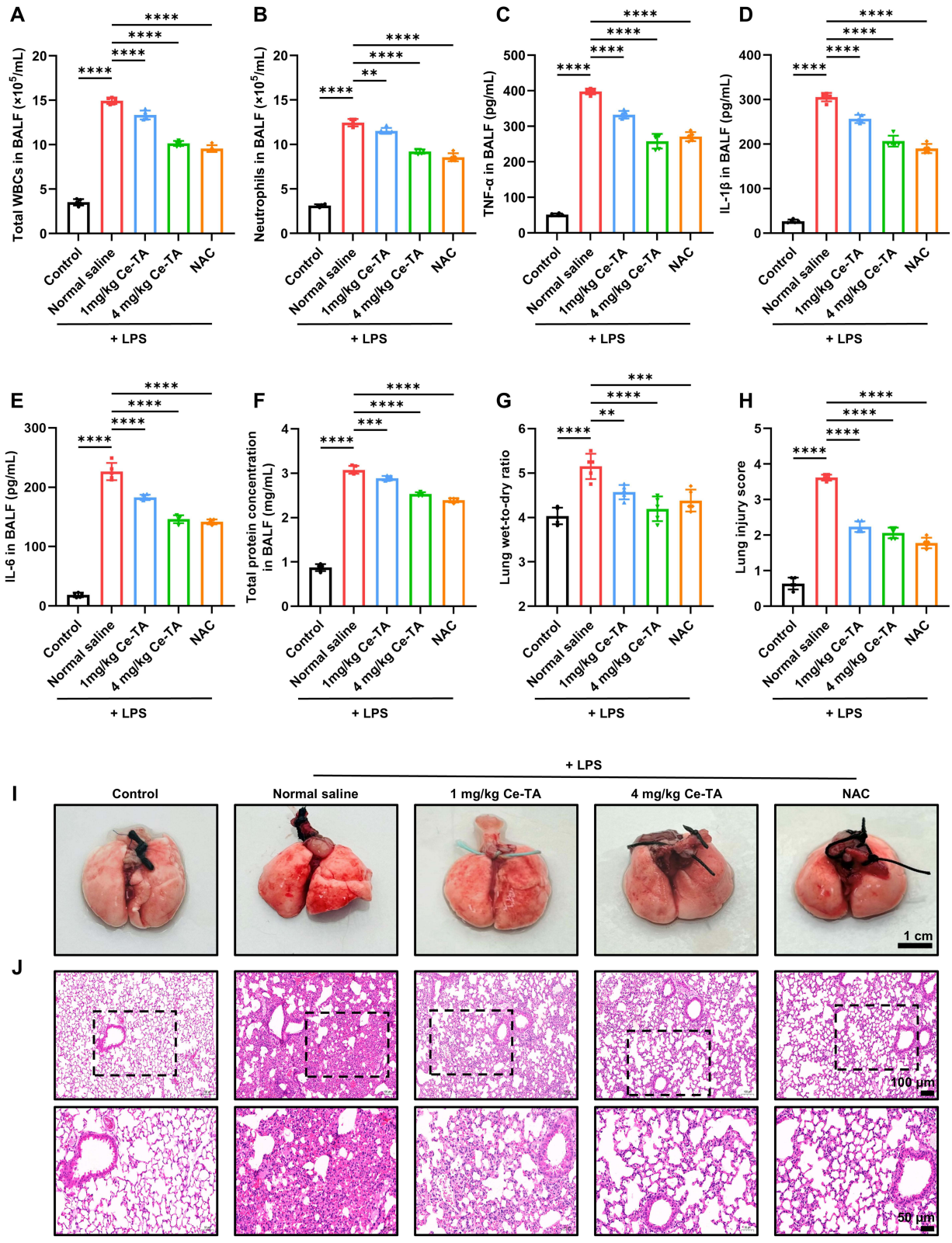

Figure 5 Therapeutic effects of Ce-TA on pulmonary inflammation and histological damage in LPS-induced ALI mice. (**A**) Total WBCs and (**B**) neutrophil counts in BALF of mice in different groups. Concentrations of (**C**) TNF-α, (**D**) IL-1β, and (**E**) IL-6 in BALF of mice in different groups. (**F**) Protein concentration in BALF of mice in different groups. (**G**) Lung wet/dry ratio of mice in different groups. (**H**) Lung injury scores calculated according to (**J**). (**I**) Representative images of lung tissues of mice in different groups. (**J**) H&E staining sections of lung tissues of mice in different groups. The content within the dotted box is displayed below the corresponding image at twice its original size. Data are presented as means ± SD (n = 5 per group). $^{**}p < 0.01$, $^{***}p < 0.001$, $^{****}p < 0.0001$.

https://doi.org/10.2147/IJN.S604112

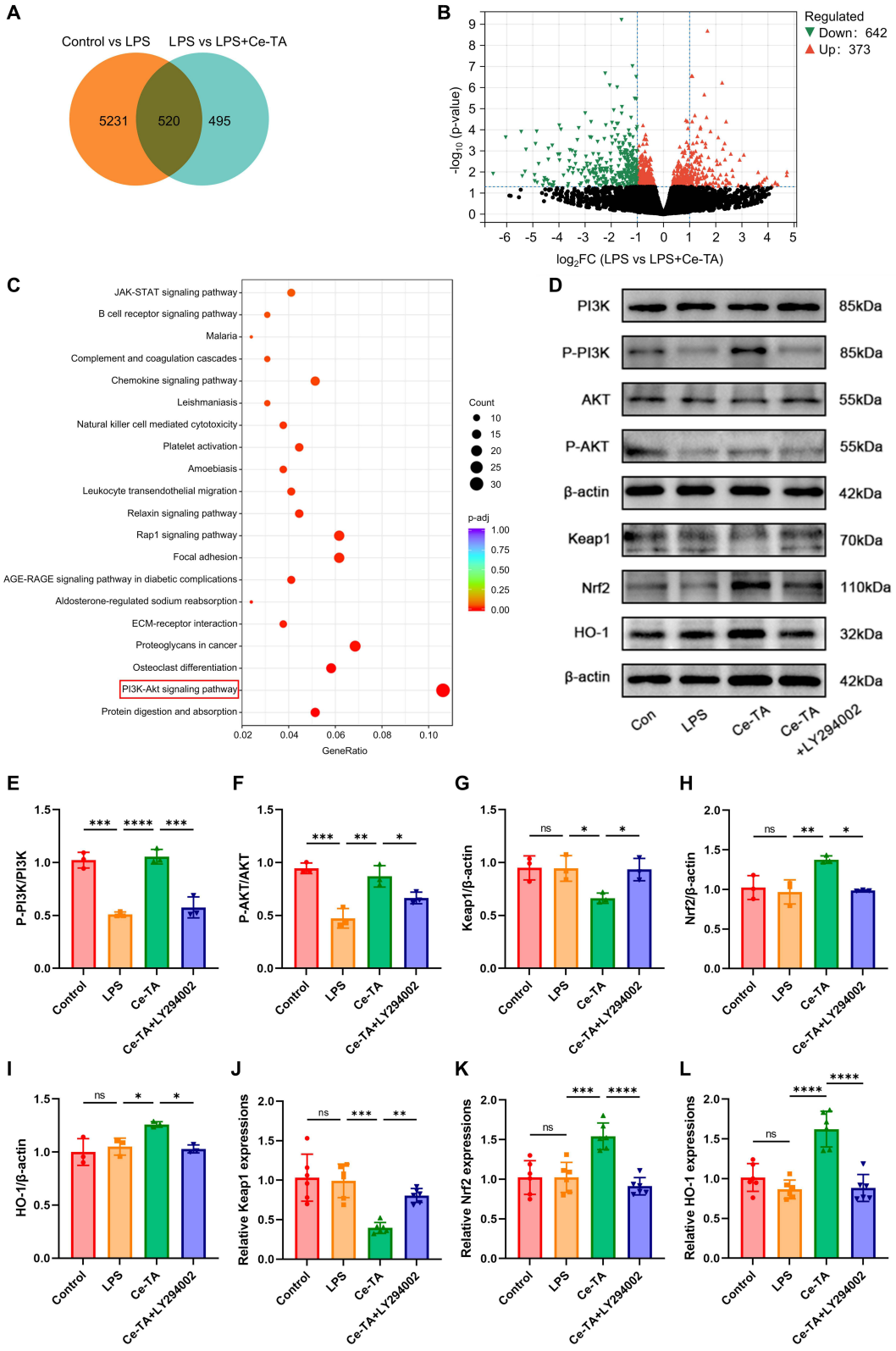

Figure 6 Ce-TA activates the PI3K/AKT/Nrf2 signaling pathway. (**A**) Venn diagram of differentially expressed genes in control, LPS, and LPS + Ce-TA group. (**B**) Volcano plot showing differentially expressed genes (fold change ≥ 1, *p*-adjust < 0.05) in LPS group versus LPS + Ce-TA group. (**C**) List of the top 20 KEGG pathways in relation to the candidate target pathways of Ce-TA-treated ALI. The red box indicates the signaling pathway with the most significant enrichment. (**D**) Western blotting of the specified proteins related to the PI3K/AKT/Nrf2 pathway in the lung tissues of mice in different groups. Quantitative analysis of (**E**) p-PI3K/PI3K, (**F**) p-AKT/AKT, (**G**) Keap1, (**H**) Nrf2, and (**I**) HO-1 protein expressions in the lung tissues of mice in different groups (n = 3 per group). mRNA levels of (**J**) Keap1, (**K**) Nrf2, and (**L**) HO-1 in the lung tissues of mice in different groups (n = 6 per group). Data are presented as means ± SD. ns, no significant difference, **p* < 0.05, ***p* < 0.01, ****p* < 0.001, *****p* < 0.0001.

https://doi.org/10.2147/IJN.S604112

To validate the effects of Ce-TA on the PI3K/AKT/Nrf2 signaling pathway, we assessed the expression of relevant proteins by Western blotting. LY294002, a PI3K inhibitor, was used to investigate whether Nrf2 activation depends on PI3K. LY294002 (3 mg/mL, i.p.) was administered 2 h before LPS stimulation, then the mice were treated with Ce-TA (4 mg/kg, i.v.) 6 h after LPS treatment. LPS-induced ALI mice were treated with normal saline or Ce-TA at 6 h after LPS stimulation. After 24 h, mice were sacrificed and lung tissues were collected. We observed that LPS injection significantly reduced p-PI3K and p-AKT expression levels compared to the control group, while Ce-TA treatment significantly upregulated p-PI3K and p-AKT expression levels compared to the LPS group. Meanwhile, the levels of p-PI3K and p-AKT were significantly lower in the Ce-TA + LY294002 group than in the Ce-TA group. No significant differences were observed in total PI3K and AKT between the groups, suggesting that Ce-TA activated the PI3K/AKT signaling pathway, while LY294002 inhibited the phosphorylation of PI3K/AKT. Furthermore, the expression levels of Nrf2 and HO-1 in the Ce-TA group were significantly higher than in the LPS group, while Keap1 expression level was significantly lower in the Ce-TA group. In contrast, the expression levels of Nrf2 and HO-1 were significantly decreased in the Ce-TA + LY294002 group in comparison with the Ce-TA group, while Keap1 level was significantly increased (Figure 6D). Quantitative analysis confirmed the above results (Figure 6E-I). Next, quantitative real-time PCR was used to detect the mRNA expression levels. As shown in Figure 6J-L, Ce-TA treatment significantly reduced the expression level of Keap1, and significantly upregulated the expression levels of Nrf2 and HO-1 in lung tissues. In addition, LY294002 partially reversed these effects of Ce-TA, demonstrating the correlation between Nrf2 activation and PI3K/AKT signaling pathway.

Immunofluorescence staining results showed stronger Nrf2 fluorescence in the Ce-TA group than in the LPS group, which was significantly decreased in the Ce-TA + LY294002 group, indicating that Nrf2 was activated by Ce-TA, whereas LY294002 reversed it (Figure 7A). Additionally, immunohistochemical staining further confirmed significantly higher Nrf2 level in the Ce-TA group compared with the LPS group, while the Nrf2 level was significantly lower in the Ce-TA + LY294002 group compared with the Ce-TA group (Figure 7C). Quantitative analysis supported the results (Figure 7B and D). These findings were consistent with the results of quantitative real-time PCR and Western blotting. Taken together, Ce-TA exerts anti-inflammatory and antioxidant effects by promoting the phosphorylation of PI3K/AKT and subsequently upregulating the Nrf2/HO-1 pathway (Scheme 1).

Safety Assessment of Ce-TA in vivo

A critical aspect of nanomaterial application is assessing their in vivo safety profile. Therefore, we conducted multiple tests to assess the safety of Ce-TA application. To evaluate the biocompatibility of Ce-TA, we first assessed its blood compatibility using red blood cells (RBCs) from healthy mice for hemolysis test. According to the results, Ce-TA induced negligible hemolysis (< 5%) at concentrations up to 1000 μg/mL, which demonstrated excellent hemocompatibility (Figure S2C). The weight of mice was recorded every 2 d over 28 d. As shown in Figure S2D, there was no significant difference in body weight between Ce-TA group and the control group, and the body weight in both groups showed an increasing trend.

Next, to assess the safety of Ce-TA on healthy mice, we randomly divided mice into two groups, including the control group and the 4 mg/kg Ce-TA (i.v.) group. Blood and tissue samples were collected at 1, 7, 14, and 28 d post-administration. Blood panel analysis showed no difference between the two groups (Figure S3A-E, Figure S5A-E, Figure S7A-E, and Figure S9A-E). The concentrations of alanine transaminase (ALT), aspartate transaminase (AST), creatinine (CREA), and blood urea nitrogen (BUN) in serum were all within normal ranges, with no significant difference observed between the groups over 28 d of observation, suggesting no observable hepatotoxicity or nephrotoxicity induced by the administration of Ce-TA (Figure S3F and G, Figure S5F and G, Figure S7F and G, and Figure S9F and G).

Moreover, H&E staining of vital organs was performed to assess potential tissue damage or inflammation. No obvious tissue damage or inflammatory response was observed in the lungs or other major organs at 1, 7, 14 and 28 d after Ce-TA administration compared to the control group (Figure S4A-C, Figure S6A-C, Figure S8A-C, and Figure S10A-C). Altogether, these results indicated that Ce-TA displayed excellent in vivo safety and supported the potential of Ce-TA as a promising therapeutic candidate for ALI.

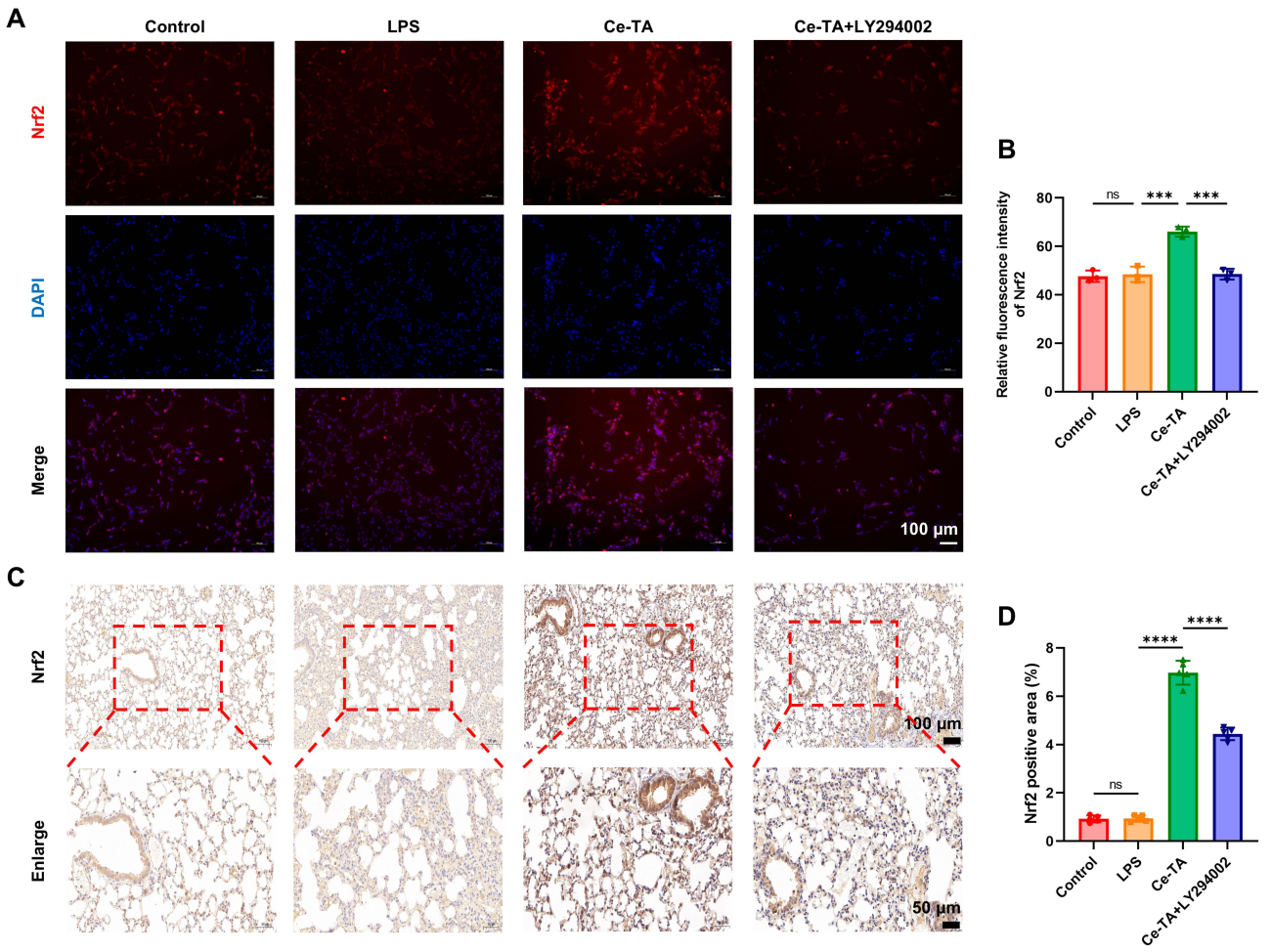

Figure 7 Ce-TA upregulates the expression level of Nrf2 through the PI3K/AKT pathway. (**A**) Representative immunofluorescence images of Nrf2 in BEAS-2B cells (n = 3 per group). (**B**) Quantitative analysis of the relative fluorescence intensity of Nrf2 in BEAS-2B cells under different treatment conditions. (**C**) Representative immunohistochemistry staining images of Nrf2 in lung tissues of mice in different groups (n = 5 per group). (**D**) Quantitative analysis of the proportion of Nrf2-positive area in lung tissues of mice in different groups. Data are presented as means ± SD. ns, no significant difference, ***$p < 0.001$, ****$p < 0.0001$.

Discussion

ALI/ARDS causes severe lung damage, leading to high global morbidity and mortality, with many patients suffering long-term sequelae. It can arise from direct causes like pneumonia and inhalation injury or indirect causes like sepsis, both leading to lung epithelial and endothelial damage, which in turn induces and dictates the severity of ARDS.[44,45] Despite significant advances in understanding the pathogenesis of ALI, effective therapeutic interventions for ALI/ARDS remain limited, with no current therapy proven to reduce mortality or improve prognosis.[46,47] Therefore, the development of effective therapeutic strategies to treat ALI/ARDS is critical. In this context, we synthesized Ce-TA nanomaterial and demonstrated that Ce-TA efficiently activated the PI3K/AKT/Nrf2 signaling pathway, thereby exerting anti-inflammatory and antioxidant effects, suggesting that Ce-TA is a promising anti-ALI therapeutic agent.

Recently, researchers have synthesized novel nanomaterials based on cerium and TA, which have demonstrated promising efficacy against inflammatory and oxidative damage.[31,38] However, the potential of Ce-TA to treat ALI has not been clarified. Here, we used TA as a ligand to synthesize Ce-TA-formaldehyde coordination polymer colloidal nanomaterials (Ce-TA) with ultra-small size and high stability. It is noteworthy that TEM reflected the diameter of nanoparticles, while AFM primarily measured the height of nanoparticles. Differences in particle sizes, as marked in Figure 1D, compared to TEM and DLS can occur due to flattening and aggregation. However, the size measured by AFM only represented local particle size and did not affect the structural characterization of the nanomaterials. We demonstrated that Ce-TA exhibited excellent ROS scavenging ability and negligible toxicity in vitro and in vivo. The dual

https://doi.org/10.2147/IJN.S604112

enzymatic activity of Ce-TA can be explained by the dynamic valence cycle between Ce^{3+} and Ce^{4+} during the catalytic process. Ce^{4+}-dominated CAT activity generates Ce^{3+} while decomposing H_2O_2, supporting SOD-like activity. TA, acting as a polyphenolic ligand, possesses inherent antioxidant properties, with phenolic hydroxyl groups acting as electron donors to reduce Ce^{4+} to Ce^{3+}, stabilizing the redox balance. Thus, the 1:2 ratio is a dynamic equilibrium that enables Ce-TA's dual enzyme-mimetic function. It also exhibited an anti-apoptotic effect in cellular models. Furthermore, we found that Ce-TA restored the expression levels of oxidative stress markers (MPO, SOD, and MDA) and decreased levels of pro-inflammatory cytokines (TNF-α, IL-1β, and IL-6) in an LPS-induced ALI mouse model. Histological analysis revealed reduced alveolar hemorrhage and inflammatory cell infiltration, attenuated pulmonary mesenchymal thickening, and recovery of normal alveolar structure after administration of Ce-TA. These findings indicated that Ce-TA inhibited ROS production in vivo and in vitro and suppressed inflammatory responses, thereby alleviating LPS-induced ALI.

We further investigated the potential mechanism underlying the effects of Ce-TA against LPS-induced ALI. Nrf2, a critical cytoprotective regulator, attenuates LPS-induced ALI by inhibiting inflammation and oxidative stress.[48] Nrf2 is primarily regulated by Keap1, which functions as a component of the Cullin3 (Cul3)-based E3 ubiquitin ligase by modulating Nrf2 ubiquitination and degradation.[49] Under normal conditions, Keap1 inhibits the transcriptional activity of Nrf2.[50] Upon external stimulation, modification of the cysteine residues in Keap1 occurs, thereby suppressing the Keap1-mediated ubiquitination of Nrf2. Consequently, Nrf2 is activated and dissociates from Keap1, translocating to the nucleus to activate downstream target genes and enhance the cellular antioxidant response.[51] Previous studies have demonstrated that various compounds can protect against multiple pathological processes by inhibiting oxidative stress and apoptosis, and alleviating inflammation through activation of the PI3K/AKT/Nrf2 signaling pathway.[52–56] According to our RNA sequencing results, the PI3K/AKT pathway is highly correlated with the mechanism of Ce-TA in the treatment of LPS-induced ALI. We found that Ce-TA significantly increased the expression levels of p-PI3K and p-AKT, and the downstream protein expression levels of Nrf2 and HO-1 were also significantly increased, whereas Keap1 expression level was significantly decreased, suggesting that Ce-TA could activate the PI3K/AKT/Nrf2 pathway to suppress inflammation and attenuate oxidative stress. Notably, the above effects of Ce-TA were significantly reversed under co-treatment with LY294002, an inhibitor of PI3K, confirming that the activation of Nrf2 is closely related to the PI3K/AKT pathway. Therefore, targeting the activation of the PI3K/AKT/Nrf2 pathway can attenuate LPS-induced ALI.

Notwithstanding the established efficacy of nanomaterials, safety and side effects are crucial issues that limit the value of their application, because the reduction in size or dimensions at nanoscale can lead not only to novel properties but also to potentially unconventional toxic behavior.[57] It is noteworthy that a certain dose of Ce-TA showed negligible toxicity in vivo and in vitro. Currently, although many molecular targets and drugs have been proposed for the treatment of ALI, the development of strategies to improve the therapeutic outcome of ALI/ARDS remains limited. Ce-TA nanomaterial has been shown to resist the inflammatory response and oxidative stress induced by LPS-mediated ALI by activating the PI3K/AKT/Nrf2 signaling pathway. We believe that it may become a promising candidate to alleviate ALI in clinical practice and lay the foundation for further development of more prospective therapeutic approaches for ALI/ARDS in the future.

Conclusions

With the continued development of nanobiotechnologies, nanomaterials have been considered for the treatment of ALI/ARDS. This study developed a Ce-TA nanomaterial with excellent antioxidant and anti-inflammatory activities, through the coordination interaction of cerium with TA. The synthesis method is facile and cost-effective. These properties make it suitable for the treatment of ALI. We confirmed that Ce-TA significantly alleviated pulmonary histopathological damage, improved alveolar-capillary barrier function, reduced inflammatory cell infiltration, and protected against LPS-induced ALI. Ce-TA activated the PI3K/AKT/Nrf2 pathway to suppress inflammatory responses and attenuate oxidative stress. This study lays a robust foundation for further exploration and development of targeted nanomaterial strategies, demonstrating the therapeutic potential of Ce-TA for ALI/ARDS and revealing a broad application prospect.

Data Sharing Statement

Data of this study will be made available from the corresponding author (Qifei Wu) upon reasonable request.

Ethics Approval and Informed Consent

All experimental procedures were conducted in accordance with institutional guidelines for the care and use of laboratory animals and protocols, which were approved by the Biomedical Ethics Committee of Health Science Center of Xi'an Jiaotong University (Granted Number: XJTUAE2024-642).

Author Contributions

All authors made a significant contribution to the work reported, whether that is in the conception, study design, execution, acquisition of data, analysis and interpretation, or in all these areas; took part in drafting, revising or critically reviewing the article; gave final approval of the version to be published; have agreed on the journal to which the article has been submitted; and agree to be accountable for all aspects of the work.

Funding

This work was funded by the National Natural Science Foundation of China (No. 82472191), Natural Science Foundation of Shaanxi Province (2024JC-ZDXM-49), and Key Research and Development Projects of Shaanxi Province (2024SF2-GJHX-45).

Disclosure

The authors declare no conflicts of interest in this paper.

References

1. Zhou M, Meng L, He Q, et al. Valsartan attenuates LPS-induced ALI by modulating NF-κB and MAPK pathways. *Front Pharmacol*. 2024;15:1321095. doi:10.3389/fphar.2024.1321095
2. Fan E, Brodie D, Slutsky AS. Acute respiratory distress syndrome: advances in diagnosis and treatment. *JAMA*. 2018;319(7):698–710. doi:10.1001/jama.2017.21907
3. Gorman EA, O'Kane CM, McAuley DF. Acute respiratory distress syndrome in adults: diagnosis, outcomes, long-term sequelae, and management. *Lancet*. 2022;400(10358):1157–1170. doi:10.1016/s0140-6736(22)01439-8
4. Huang Z, Wang Y, Yao D, et al. Nanoscale coordination polymers induce immunogenic cell death by amplifying radiation therapy mediated oxidative stress. *Nat Commun*. 2021;12(1):145. doi:10.1038/s41467-020-20243-8
5. Zhang S, Zhang S, Luo S, Wu D. Therapeutic agent-based infinite coordination polymer nanomedicines for tumor therapy. *Coordin Chem Rev*. 2021;445:214059. doi:10.1016/j.ccr.2021.214059
6. García-Pardo J, Novio F, Nador F, et al. Bioinspired theranostic coordination polymer nanoparticles for intranasal dopamine replacement in Parkinson's disease. *ACS Nano*. 2021;15(5):8592–8609. doi:10.1021/acsnano.1c00453
7. Chen L, Peng M, Li H, et al. Metal-phenolic network with Pd nanoparticle nodes synergizes oxidase-like and photothermal properties to eradicate oral polymicrobial biofilm-associated infections. *Adv Mater*. 2024;36(7):e2306376. doi:10.1002/adma.202306376
8. Yu R, Chen H, He J, et al. Engineering antimicrobial metal–phenolic network nanoparticles with high biocompatibility for wound healing. *Adv Mater*. 2024;36(6):e2307680. doi:10.1002/adma.202307680
9. Li Y, Miao Y, Yang L, et al. Recent advances in the development and antimicrobial applications of metal–phenolic networks. *Adv Sci*. 2022;9(27):e2202684. doi:10.1002/advs.202202684
10. Zhang X, Li Z, Yang P, et al. Polyphenol scaffolds in tissue engineering. *Mater Horiz*. 2021;8(1):145–167. doi:10.1039/d0mh01317j
11. Zhu W, Guo J, Ju Y, et al. Modular metal–organic polyhedra superassembly: from molecular-level design to targeted drug delivery. *Adv Mater*. 2019;31(12):e1806774. doi:10.1002/adma.201806774
12. Qin J, Liang G, Feng Y, et al. Synthesis of gadolinium/iron–bimetal–phenolic coordination polymer nanoparticles for theranostic applications. *Nanoscale*. 2020;12(10):6096–6103. doi:10.1039/c9nr10020b
13. Feng Y, Li P, Wei J. Engineering functional mesoporous materials from plant polyphenol based coordination polymers. *Coordin Chem Rev*. 2022;468:214649. doi:10.1016/j.ccr.2022.214649
14. Pei H, Bai Y, Guo J, et al. Tunable morphologies of polymer capsules templated from cuprous oxide particles for control over cell association. *Chinese Chem Lett*. 2020;31(2):505–508. doi:10.1016/j.cclet.2019.04.049
15. Meng J, Wang L, Zou B, et al. Fluorescent-based nanoplatform with real-time quantification of drug release. *ACS Appl Polym Mater*. 2023;5(2):1539–1544. doi:10.1021/acsapm.2c02025
16. Jiang W, Wang Q, Cui D, et al. Metal-polyphenol network coated magnetic hydroxyapatite for pH-activated MR imaging and drug delivery. *Colloids Surf B Biointerfaces*. 2023;222:113076. doi:10.1016/j.colsurfb.2022.113076
17. Zhang Z, Xie L, Ju Y, Dai Y. Recent advances in metal-phenolic networks for cancer theranostics. *Small*. 2021;17(43):e2100314. doi:10.1002/smll.202100314
18. Liu P, Shi X, Zhong S, et al. Metal-phenolic networks for cancer theranostics. *Biomater Sci*. 2021;9(8):2825–2849. doi:10.1039/d0bm02064h
19. Qin J, Liang G, Feng B, et al. Facile synthesis of metal-polyphenol-formaldehyde coordination polymer colloidal nanoparticles with sub-50 nm for T1-weighted magnetic resonance imaging. *Chinese Chem Lett*. 2021;32(2):842–848. doi:10.1016/j.cclet.2020.05.021
20. Qin J, Liang G, Cheng D, et al. Controllable synthesis of iron-polyphenol colloidal nanoparticles with composition-dependent photothermal performance. *J Colloid Interface Sci*. 2021;593:172–181. doi:10.1016/j.jcis.2021.02.082

21. Cui J, Alt K, Ju Y, et al. Ligand-functionalized Poly(ethylene glycol) particles for tumor targeting and intracellular uptake. *Biomacromolecules*. 2019;20(9):3592–3600. doi:10.1021/acs.biomac.9b00925
22. Yun G, Richardson JJ, Biviano M, Caruso F. Tuning the Mechanical behavior of metal–phenolic networks through building block composition. *ACS Appl Mater Interfaces*. 2019;11(6):6404–6410. doi:10.1021/acsami.8b19988
23. Dong Z, Feng L, Chao Y, et al. Amplification of tumor oxidative stresses with liposomal fenton catalyst and glutathione inhibitor for enhanced cancer chemotherapy and radiotherapy. *Nano Lett*. 2019;19(2):805–815. doi:10.1021/acs.nanolett.8b03905
24. Zhao Y, Zeng H, Zhu X-W, et al. Metal–organic frameworks as photoluminescent biosensing platforms: mechanisms and applications. *Chem Soc Rev*. 2021;50(7):4484–4513. doi:10.1039/d0cs00955e
25. Chircov C, Mincă M-A, Serban AB, et al. Zinc/Cerium-substituted magnetite nanoparticles for biomedical applications. *Int J Mol Sci*. 2023;24 (7):6249. doi:10.3390/ijms24076249
26. Zandi M, Hosseini F, Adli AH, et al. State-of-the-art cerium nanoparticles as promising agents against human viral infections. *Biomed Pharmacother*. 2022;156:113868. doi:10.1016/j.biopha.2022.113868
27. Rajeshkumar S, Naik P. Synthesis and biomedical applications of Cerium oxide nanoparticles – a Review. *Biotechnol Rep*. 2017;17:1–5. doi:10.1016/j.btre.2017.11.008
28. Liu H-J, Wang M, Wang Y, et al. Ceria nanocluster-based therapy for Alzheimer's disease through the modulation of activated microglia and attenuation of amyloid-β deposition. *Cell Biomaterials*. 2025;1(10):100158. doi:10.1016/j.celbio.2025.100158
29. Zhang X, Yan Y, Li N, et al. A robust and 3D-printed solar evaporator based on naturally occurring molecules. *Sci Bull*. 2023;68(2):203–213. doi:10.1016/j.scib.2023.01.017
30. Fu H, Wang Y, Huang B, et al. Tannic acid-cerium nanoenzymes serve as broad-spectrum antioxidants to alleviate acute kidney injury by modulating macrophage polarization, mitophagy and endoplasmic reticulum stress. *J Control Release*. 2025;380:892–909. doi:10.1016/j.jconrel.2025.02.038
31. Peng W, Tai W, Li B, et al. Inhalable nanocatalytic therapeutics for viral pneumonia. *Nat Mater*. 2025;24(4):637–648. doi:10.1038/s41563-024-02041-5
32. Liu S, Bao J, Tian B, et al. Piezoelectric bilayer Nickel-Iron layered double hydroxide nanosheets with tumor microenvironment responsiveness for intensive piezocatalytic therapy. *Adv Sci*. 2024;11(39):e2404146. doi:10.1002/advs.202404146
33. Yang L, Liu S, Yang M, et al. Manganese-Doped piezoelectric layered double hydroxides induce catalytic therapy and ferroptosis. *Adv Funct Mater*. 2026;36:e31699. doi:10.1002/adfm.202531699
34. Liu S, Wang C, Wang C, et al. A biodegradable self-cascading copper-based nanozyme for augmented cancer catalytic therapy and cuproptosis. *J Colloid Interface Sci*. 2026;701:138692. doi:10.1016/j.jcis.2025.138692
35. Zhang L, Liu S, Xu J, et al. Hydrogenated FeMo nanozymes with tannin networks-enabled targeting delivery for NIR-II-intensified tumor therapy. *Chem Eng J*. 2026;532:174410. doi:10.1016/j.cej.2026.174410
36. Liu M, Cai C, Li J, et al. Stöber synthesis of tannic acid–formaldehyde resin polymer spheres and their derived carbon nanospheres and nanocomposites for oxygen reduction reaction. *J Colloid Interface Sci*. 2018;528:1–9. doi:10.1016/j.jcis.2018.05.070
37. Daré RG, Kolanthai E, Neal CJ, et al. Cerium oxide nanoparticles conjugated with tannic acid prevent UVB-induced oxidative stress in fibroblasts: evidence of a promising anti-photodamage agent. *Antioxidants*. 2023;12(1):190. doi:10.3390/antiox12010190
38. Chen X, He Q, Zhai Q, et al. Adaptive nanoparticle-mediated modulation of mitochondrial homeostasis and inflammation to enhance infected bone defect healing. *ACS Nano*. 2023;17(22):22960–22978. doi:10.1021/acsnano.3c08165
39. Yan J, Tang Z, Li Y, et al. Molybdenum nanodots for acute lung injury therapy. *ACS Nano*. 2023;17(23):23872–23888. doi:10.1021/acsnano.3c08147
40. Lin W, Chen H, Chen X, Guo C. The roles of neutrophil-derived myeloperoxidase (MPO) in diseases: the new progress. *Antioxidants*. 2024;13 (1):132. doi:10.3390/antiox13010132
41. Zhang DD. Thirty years of NRF2: advances and therapeutic challenges. *Nat Rev Drug Discov*. 2025;24(6):421–444. doi:10.1038/s41573-025-01145-0
42. Zhang B, Zeng M, Li B, et al. Arbutin attenuates LPS-induced acute kidney injury by inhibiting inflammation and apoptosis via the PI3K/Akt/Nrf2 pathway. *Phytomedicine*. 2021;82:153466. doi:10.1016/j.phymed.2021.153466
43. Zhou L, Xu H, Lei X, et al. Coptisine mitigates acute lung injury by alleviating ferroptosis through the PI3K/AKT/Nrf2 pathway. *J Ethnopharmacol*. 2026;354:120472. doi:10.1016/j.jep.2025.120472
44. Wick KD, Ware LB, Matthay MA. Acute respiratory distress syndrome. *BMJ*. 2024;387:e076612. doi:10.1136/bmj-2023-076612
45. Bos LDJ, Ware LB. Acute respiratory distress syndrome: causes, pathophysiology, and phenotypes. *Lancet*. 2022;400(10358):1145–1156. doi:10.1016/S0140-6736(22)01485-4
46. Yang L, Luo W, Zhang Q, et al. Cardamonin inhibits LPS-induced inflammatory responses and prevents acute lung injury by targeting myeloid differentiation factor 2. *Phytomedicine*. 2021;93:153785. doi:10.1016/j.phymed.2021.153785
47. He Y-Q, Zhou -C-C, Yu L-Y, et al. Natural product derived phytochemicals in managing acute lung injury by multiple mechanisms. *Pharmacol Res*. 2021;163:105224. doi:10.1016/j.phrs.2020.105224
48. Lee J, Jang J, Park S-M, Yang S-R. An update on the role of Nrf2 in respiratory disease: molecular mechanisms and therapeutic approaches. *Int J Mol Sci*. 2021;22(16):8406. doi:10.3390/ijms22168406
49. Itoh K, Wakabayashi N, Katoh Y, et al. Keap1 represses nuclear activation of antioxidant responsive elements by Nrf2 through binding to the amino-terminal Neh2 domain. *Genes Dev*. 1999;13(1):76–86. doi:10.1101/gad.13.1.76
50. Kobayashi A, Kang M-I, Okawa H, et al. Oxidative stress sensor Keap1 functions as an adaptor for Cul3-Based E3 ligase to regulate proteasomal degradation of Nrf2. *Mol Cell Biol*. 2004;24(16):7130–7139. doi:10.1128/mcb.24.16.7130-7139.2004
51. O'Rourke SA, Shanley LC, Dunne A. The Nrf2-HO-1 system and inflammaging. *Front Immunol*. 2024;15:1457010. doi:10.3389/fimmu.2024.1457010
52. Yu B, Wang Q, Zhang L, et al. Ebselen improves fungal keratitis through exerting anti-inflammation, anti-oxidative stress, and antifungal effects. *Redox Biol*. 2024;73:103206. doi:10.1016/j.redox.2024.103206
53. Li Y, Chen L, Zheng D, et al. Echinocystic acid alleviated hypoxic-ischemic brain damage in neonatal mice by activating the PI3K/Akt/Nrf2 signaling pathway. *Front Pharmacol*. 2023;14:1103265. doi:10.3389/fphar.2023.1103265

54. Huang M, Yan Y, Deng Z, et al. Saikosaponin A and D attenuate skeletal muscle atrophy in chronic kidney disease by reducing oxidative stress through activation of PI3K/AKT/Nrf2 pathway. *Phytomedicine*. 2023;114:154766. doi:10.1016/j.phymed.2023.154766
55. Wen X, Tang S, Wan F, et al. The PI3K/Akt-Nrf2 signaling pathway and mitophagy synergistically mediate hydroxytyrosol to alleviate intestinal oxidative damage. *Int J Biol Sci*. 2024;20(11):4258–4276. doi:10.7150/ijbs.97263
56. Li D, Zhao Z, Zhu L, et al. 7,8-DHF inhibits BMSC oxidative stress via the TRKB/PI3K/AKT/NRF2 pathway to improve symptoms of postmenopausal osteoporosis. *Free Radic Biol Med*. 2024;223:413–429. doi:10.1016/j.freeradbiomed.2024.08.014
57. Ma X, Tian Y, Yang R, et al. Nanotechnology in healthcare, and its safety and environmental risks. *J Nanobiotechnol*. 2024;22(1):715. doi:10.1186/s12951-024-02901-x